ELSEVIER

Journal of Structural Geology 30 (2008) 746–760

JOURNAL OF STRUCTURAL GEOLOGY

www.elsevier.com/locate/jsg

3D seismic characterisation of an array of blind normal faults in the Levant Basin, Eastern Mediterranean

Catherine Baudon*, Joe A. Cartwright

3D Laboratory, School of Earth, Ocean and Planetary Sciences, Cardiff University, Main Building, Park Place, Cardiff CF10 3AT, UK

Received 14 December 2006; received in revised form 7 December 2007; accepted 18 December 2007
Available online 6 January 2008

Abstract

The geometry, throw distribution and kinematics of an array of blind normal faults were investigated using a high resolution 3D seismic dataset located in the Levant Basin, offshore Israel, to establish criteria allowing true blind faults to be distinguished from minor synsedimentary faults. A detailed analysis of throw distribution on the fault planes shows that the displacement exhibits a crudely concentric pattern about a maximum region located centrally on a fault plane, as expected for ideal blind faults. However, vertical displacement profiles do not exhibit classical linear or triangular profiles but are mostly flat-topped or hybrid in type. Comparison of unrestricted blind faults to those that interacted with a mechanical boundary or another structure suggests that such interactions significantly modify the throw spatial distribution on a fault plane. To distinguish small synsedimentary faults from blind faults, we use a combination of three criteria to assess whether a fault grew by blind propagation: (1) plunging upper-tip region and complementary pattern in the throw contours, (2) presence of upper-tip propagation fold, and (3) absence of stratigraphic evidence that the fault interacted with the free surface.

Keywords: Blind fault; Throw distribution; Fault propagation; Fault growth; Lithological effects; Mechanical stratigraphy

1. Introduction

The analysis of displacement distribution on fault surfaces has provided significant insights into the nucleation and propagation of faults (e.g. Childs et al., 1993; Dawers and Anders, 1995). The early work was based on the characteristics of an ideal blind normal fault defined as a fault that does not intersect a free surface (Watterson, 1986). In this ideal model, displacement decreases from a maximum located at the centre of the fault plane to a tip line of zero displacement. In the absence of significant mechanical heterogeneity and if displacement accrued over the entire fault plane at each slip event, the tip line is elliptical. Ideal blind faults grow by radial propagation with no migration of the point of maximum displacement, which is also the nucleation site of the fault (Watterson, 1986; Barnett et al., 1987).

This model has also been modified to include the role of segment linkage (Peacock and Sanderson, 1991; Cartwright et al., 1995; Dawers and Anders, 1995; Wojtal, 1996), the influence of mechanical heterogeneity (Peacock and Zhang, 1994; Mansfield and Cartwright, 1996; Gross et al., 1997; Wilkins and Gross, 2002) and mechanical interactions with other structures during propagation (Nicol et al., 1996; Maerten et al., 1999).

Numerous studies published data from normal faults considered as mostly post-sedimentary (e.g. Walsh and Watterson, 1987, 1988a; Gillespie et al., 1993; Watterson et al., 1998). However, few published descriptions exist for displacement distribution on entire fault planes from seismic data (Table 1). Another issue of interest is that the displacement patterns of small synsedimentary faults that have slow and regular displacement rates can be remarkably similar to those of ideal blind faults, adding to the complexity of interpretation (e.g. Petersen et al., 1992; Childs et al., 1993; Nicol et al., 1996).

* Corresponding author. NARG, SEAES, The University of Manchester, Oxford Road, Williamson Building, Manchester M13 9PL, UK. Tel.: +44 (0)161 275 0778; fax.: +44 (0)161 306 9361.
E-mail address: catherine.baudon@manchester.ac.uk (C. Baudon).

0191-8141/$ - see front matter © 2007 Elsevier Ltd. All rights reserved.
doi:10.1016/j.jsg.2007.12.008

Table 1
Blind faults with entire fault plane in the literature from seismic data

Source	Data	Measurements	Dimension	D_{max}
Barnett et al., 1987	Offshore UK North Sea (2D seismic)	52 vertical displacement measurements on 4 mapped reflectors	$L \sim 1220$ m	45 ms
Walsh and Watterson, 1991	Offshore oilfield (2D seismic)	62 displacement measurements on 4 mapped reflectors 100 m spacing between seismic lines	$L = 1800$m	60 m
Nicol et al., 1996	Gulf Coast (3D seismic)	106 throw readings on 5 horizons Estimation of tip lines positions by extrapolation of throw gradients	$L = 1500$ m $H \sim 1500$ m	42 ms = 53 m
Nicol et al., 2003	South Australia (3D seismic)	3 throw contour plots of restricted faults	Various	Various

This paper investigates a system of small normal faults using high resolution 3D seismic data to propose criteria for determining if a fault is truly blind. This question is important for those involved in dating the duration of faulting, since the dating of blind faults differs from the dating of synsedimentary faults due to the absence of growth sediments.

The examples of blind faults in this paper are located in the Levant Basin in the eastern Mediterranean. The faults show varying degrees of interaction with neighbouring faults, and varying relationships with the mechanical stratigraphy, thus allowing their effects on throw accumulation to be calibrated.

2. Regional setting

The study area is located in the Levant Basin in the eastern Mediterranean (Fig. 1). The basin formed by rifting during the Early Permian to the middle Jurassic during the evolution of the Neo-Tethys Ocean (Garfunkel, 1998). Located at the zone of interaction between the Anatolian, African and Arabian plates, its evolution is influenced by the Dead Sea Transform to the East, the Gulf of Suez to the SW, the Cyprian Arc to the NW, Taurus mountains and Bitlis suture to the North (Tibor and Ben-Avraham, 2005). A motion change in the Late Cretaceous between African and Eurasian plates led to a compressive stress-regime and induced a change in the depositional systems (Tibor and Ben-Avraham, 1992; Druckman et al., 1995). In the Late Miocene, a major desiccation of the Mediterranean region, the Messinian Salinity Crisis, led to the deposition of thick evaporites in the basin floor regions (Tibor and Ben-Avraham, 1992), pinching out laterally against basin margins as a function of structure and relict topography (Bertoni and Cartwright, 2006).

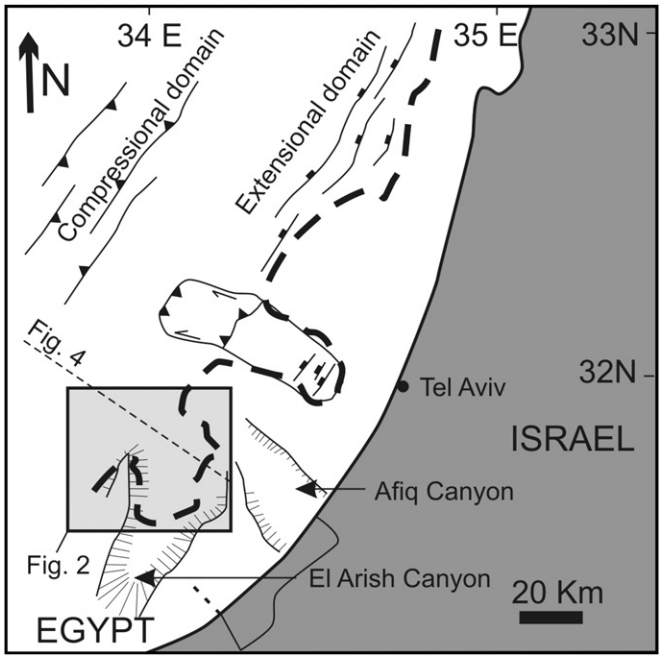

Fig. 1. Location map of the study area (grey square situates Fig. 2), offshore Israel. The dashed line represents the margin of the Messinian evaporites.

The Pliocene–Quaternary succession above the Messinian unconformity is the focus of this study. During the Pliocene, a major transgression led to the deposition of an important accumulation of clay-rich marls, sandstones and claystones mainly derived from the Nile Delta (Tibor and Ben-Avraham, 1992; Frey Martinez et al., 2005). Abrupt tilting of the margin beginning in the mid-late Pliocene resulted in two scales of gravity-driven deformation, thin-skinned sliding and slumping of slope units (Frey Martinez et al., 2005) and more substantial gravitational collapse rooted in the thick Messinian evaporites (Garfunkel and Almagor, 1987; Netzeband et al., 2006; Cartwright and Jackson, 2008). This latter deformation produced an updip extensional domain at the pinch-out of the Messinian evaporites, and a downdip contractional domain in the basin floor region (Gradmann et al., 2005). The extensional domain is characterised by a series of downslope and upslope dipping extensional faults (Fig. 1).

The study area is located in the southern part of this extensional domain, where the depositional edge of the Messinian evaporite basin defines a 'salt salient' from the interplay between the Messinian base levels and the relict topography of a series of pre-Messinian submarine canyons (Bertoni and Cartwright, 2006). The study area involves one of these canyons (called the El Arish) and the extensional domain is bounded by Messinian evaporite pinch-out around this canyon salient (Bertoni and Cartwright, 2006).

3. Database, methods and limitations

The main database for this study is a high-resolution 3D seismic survey located in the southern part of the Levant Basin

(Fig. 1). The 3D coverage amounts to 2200 km^2 with excellent stratigraphic resolution. The frequency ranges between 35-80 Hz with a dominant frequency of 50 Hz at the base of the Pliocene, giving a vertical stratigraphic resolution of c. 10 m. The spatial resolution is approximately equivalent to the bin size of 25 m. Ten exploration wells drilled in the survey area include the key wells Gaza-marine 1 and Gaza-marine 2 (Fig. 2), provided standard petrophysical data and velocity data for time-to-depth conversion.

Fault and horizon interpretation and throw mapping were conducted on a UNIX workstation using Schlumberger Geoframe 3.7 seismic interpretation software. Throw values were measured on extensional faults using seismic profiles orthogonal to fault strike and displayed as throw versus depth plots (T–z plots, Cartwright et al., 1998), lateral profiles and as contoured fault plane projections (following standard techniques outlined by Barnett et al., 1987).

To simplify the analysis, T–z plots were displayed in values of two-way travel-time (TWT). To verify whether this substitution would introduce significant distortion to the pattern of vertical throw variation, faults closest to the control wells were depth converted using check-shot velocity data from nearby control wells. Depth converted T–z plots in Fig. 3 exhibit a strikingly similar overall pattern in depth and time.

Maximum errors in the throw measurement are estimated to be a fixed value of 2 ms TWT. The distinctive character of the marker horizons and the ability to tie these horizons continuously around lateral fault tips eliminates correlation error. Hence, the only error in direct throw measurement is due to the sampling interval of the seismic data, which is 2 ms TWT. The sampling interval determines accuracy when matching two correlative seismic reflection peaks or troughs, not the vertical stratigraphic resolution, as is sometimes mistakenly assumed. Errors due to differential compaction between hangingwall and footwall are negligible because of the small throw values (Mansfield, 1996; Cartwright et al., 1998). Fault drag can also introduce errors for displacement measurements (e.g. Walsh and Watterson, 1987; Mansfield and Cartwright, 1996). True drag folds cannot generally be distinguished from seismic imaging artefacts when the fold wavelength is less than 2–3 times the spatial resolution. Drag folds with wavelengths of c. <100 m were therefore included in the throw measurements for all faults. Throw measurements were made at the inflection points closest to the apparent hanging wall and footwall cut-offs (Mansfield and Cartwright, 1996).

Our study is based exclusively on seismic data and is therefore subject to the usual caveats regarding seismic resolution. The interpretation of upper-tip regions deserves special mention as subseismic faults being could occur in apparent continuous folds on the seismic data without detection. Our interpretation of tip folds is restricted to structures where visible systematic offset of reflections is absent across a zone at least three traces in width (75 m). Observation of fault offset invariably passes systematically upward into a region where reflections are deflected, but not offset, and this fold can be traced with confidence because of the close spacing of the 3D seismic profiles. The upper-tips are located at the point where stratal deflection is no longer detectable. Subseismic faults can continue upwards beyond this limit (the 'seismic' upper-tip), but in the shallow subsurface with our high resolution data, the minimum detectable limit of deflection is less than 2 ms TWT (c. 1.5 m).

4. The El Arish fault array

4.1. Structural and stratigraphic setting

The main structures within the Levant survey area (Fig. 2a) include the western and eastern graben systems, respectively called Shamir and Kefira for the purpose of the

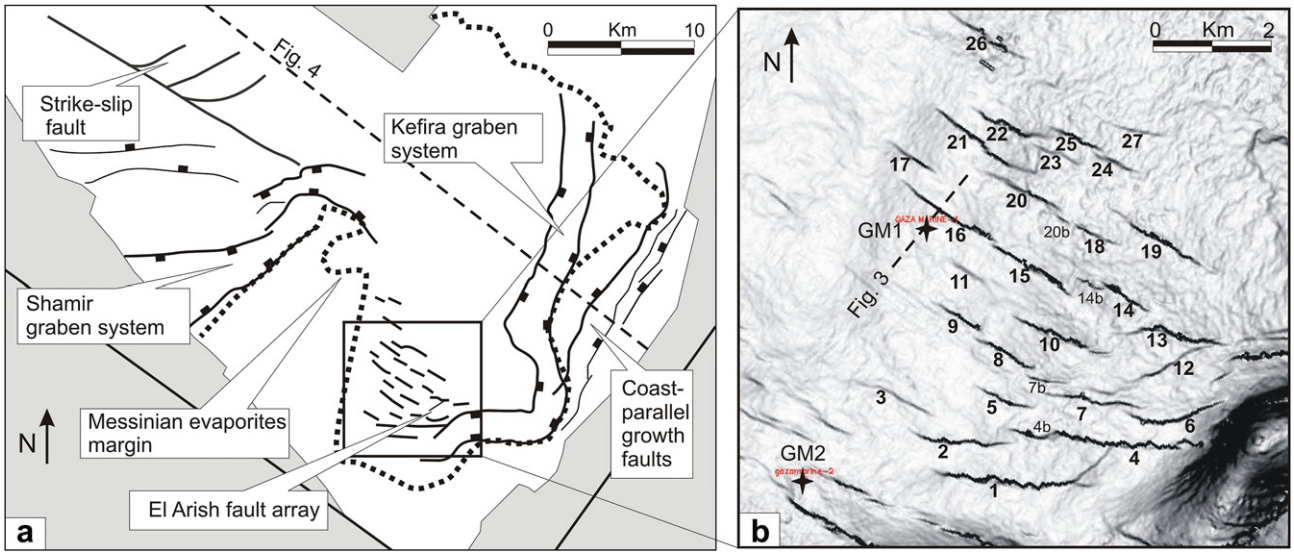

Fig. 2. (a) Structural map of the Levant survey based on a Pleistocene horizon. (b) Dip map showing the El Arish fault array and location of wells Gaza-marine 1 and 2 (GM1 and GM2).

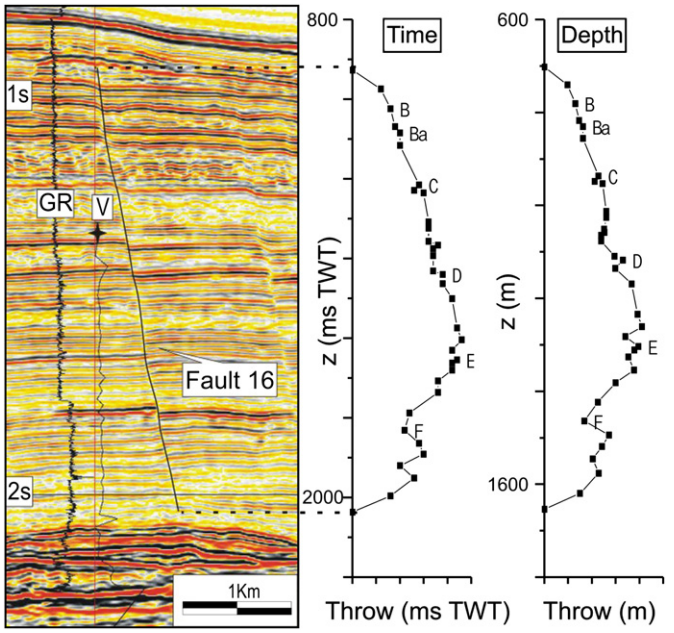

Fig. 3. Seismic section showing Gamma Ray (GR) and Velocity (V) profiles from well Gaza-Marine 1 in the proximity of Fault 16. Star symbol marks the uphole limit of velocity data.

study. These consist of complex arrays of oppositely dipping normal faults that strike approximately parallel to the pinchout of the Messinian evaporites. Individual faults defining these grabens have throws of up to 400 m and have been active from the late Pliocene. The northeastern limit of the Shamir graben system is located at proximity of a major WSW-striking strike-slip fault that also detached within the Messinian evaporites. The Kefira graben system dies out in a northeasterly direction along the trace of the evaporite pinchout and to the southwest its strike swings around to WNW direction at the head of the salient. At this position, the well defined graben bounding faults end and are replaced by the El Arish fault array, consisting of a set of WNW-striking small extensional faults. These faults strike perpendicular to the local slope direction defined at the regional detachment level and thus appear to represent a continuation of the extensional domain into the western margin of the salient. The strikes of individual faults are aligned with respect to the slope of the underlying detachment as typical for gravity-driven deformation (Jackson, 1995).

The faults of the El Arish array offset clay-rich marls, sandstones and claystones of Plio-Pleistocene age and generally tip-out downward just above the top of the Messinian evaporite succession (Fig. 4). The Messinian evaporites are recognised by two high amplitude continuous seismic reflections (Horizons M and N, Bertoni and Cartwright, 2006), and consist mainly of halite in the basinal facies with interbeds of anhydrite, halite and thin claystones. The post-Messinian Yafo Marl Member (YMM) at the base of the Pliocene consists of marls interbedded with thin sandstones and siltstones. Locally, they are overlain by the Yafo Sand Member (YSM) consisting of sandstones interbedded with thin claystones and marls. The Plio-Pleistocene sediments above the YSM are a focus of this paper. They are characterised by closely spaced, highly continuous seismic reflections, which is ideal for correlation and throw measurement. These

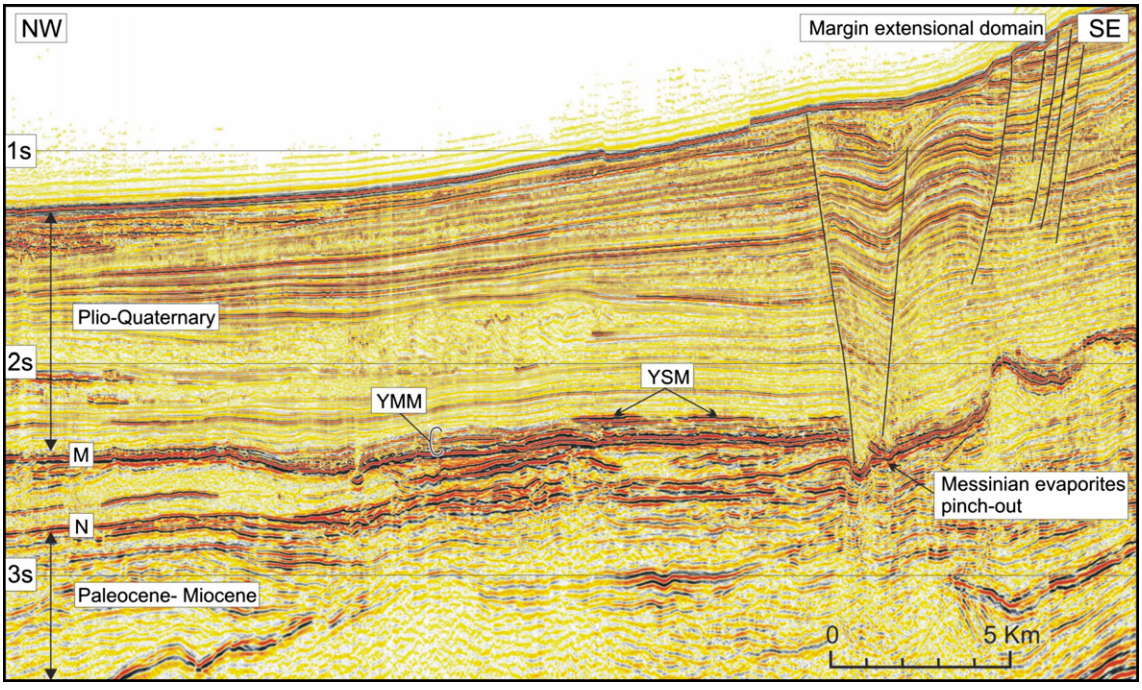

Fig. 4. Regional seismic section across the Levant Basin continental margin showing the main stratigraphic units including Yafo Marls Member (YMM) and Yafo Sand Member (YSM). Horizons M and N respectively indicate top and base of the Messinian evaporites. Profile located in Fig. 2a.

sediments are mostly claystones interbedded with limestones, sandstones and siltstones.

4.2. The El Arish fault array

The array consists of over 50 small extensional faults of which 30 located at the southern end of the array were studied (Fig. 2b). The majority of the faults dip downslope, except antithetic faults 11, 12, 20 and 26. The mapped fault traces are crudely linear, and 1–3 km in length, and up to 1.3 km in height. Average dips range from 50° to 60° and maximum throw values from 7 to 40 m. The upper-tips terminate at different stratigraphic intervals within the Pleistocene, and the lower-tips are located within the Lower Pliocene, or less commonly within the uppermost Messinian.

Mapping of 14 marker horizons across a 1000 m interval shows that hard linkages between faults with separations of greater than 100 m are rare. Strong curvature of a lateral tip towards a neighbouring fault is only seen for Fault 1 (Fig. 2b). Faults 17 and 26 show no interaction with other seismically resolvable structures, have upper-tips situated several hundreds of metres below the seabed and basal tips located above the Messinian evaporites. Fault 17 is interpreted as a unrestricted fault (Nicol et al., 1996) and is used as a reference example in the next section to compare with three examples of restricted blind faults (faults 19, 15/16 and 21) with different degrees of interaction to neighbouring faults or major lithological boundaries (Figs. 5–11).

4.3. General description of case study faults

Seismic attribute analysis of mapped horizons bracketing the upper half of the four fault planes shows no geomorphological or stratigraphic evidence that the faults interacted with the free surface at any point during their growth history. For instance, they lack evidence of fault scarps, nor is any change observed in the size, geometry or orientation of channels or slump units that are offset by the faults. In the light of these observations and of the following displacement analysis, these faults are interpreted as blind.

No seismically resolvable antithetic or synthetic faults interact with Fault 17. Small antithetic faults intersect with the lower-tip regions of Faults 19 and 15/16 but result in no significant perturbation of the throw distribution (Figs. 8 and 10). The SE upper-tip region of Fault 21 abuts against antithetic Fault 20.

The upper-tip lines of the four faults are located at least 200 ms TWT (c. 175 m) beneath the present-day seabed. Importantly, these tip-lines plunge by between 150 and 500 ms TWT (c. 130–450 m) towards the lateral tip regions.

The lower-tip lines of the four faults are mainly in the basal Pliocene units, i.e. above the regional detachment level of the Top Messinian (Cartwright and Jackson, 2008). Fault 17 tips out a few tens of metres above the YSM (Fig. 5c), and Faults 15/16 and 21 tip-out at the top of the YSM. In contrast, Fault 19 tips out within the YSM or the uppermost Messinian evaporites, but only along the central part of the fault. The basal tip-lines of these three latter faults become progressively

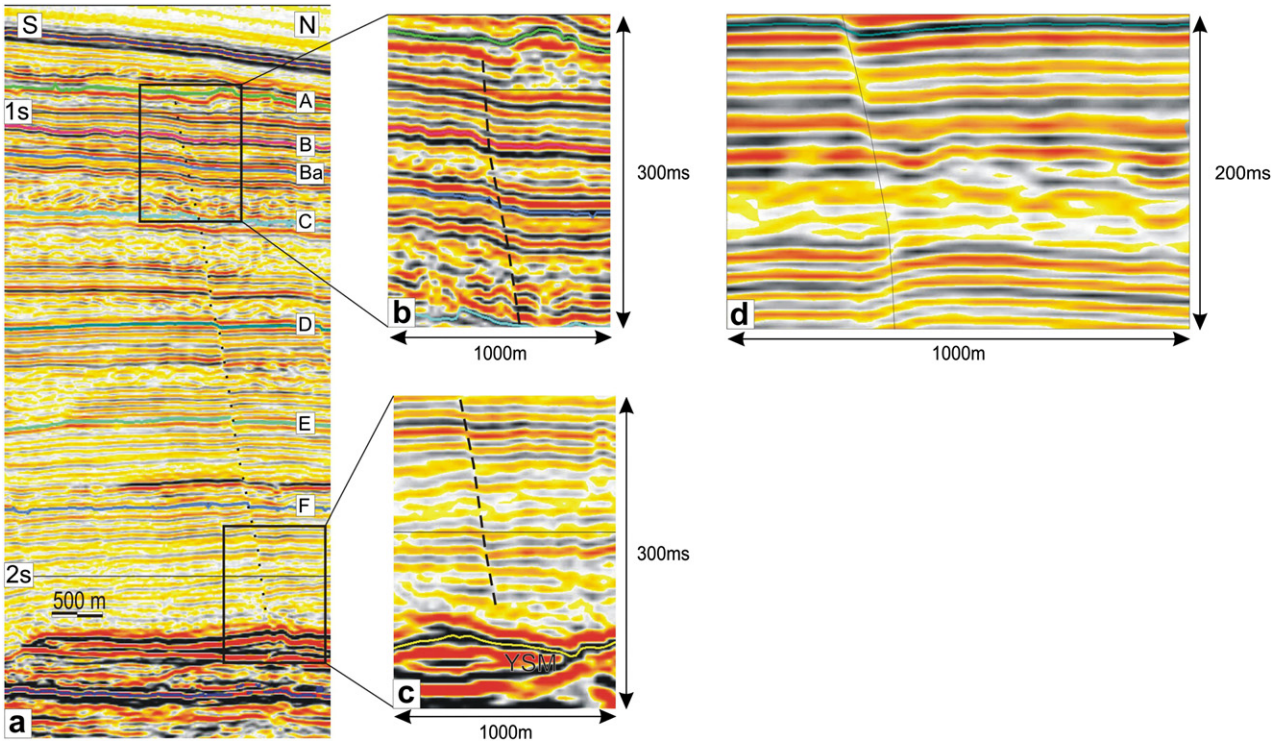

Fig. 5. (a) Seismic section across Fault 17 shows the position of upper and lower-tips and small magnitude of displacement over the fault height. Key horizons are labelled A–F. (b) Close-up showing the significant upper-tip folding. (c) Close-up showing the lower-tip terminating just above the YSM. (d) Very small amplitude or negligible reverse-drag folding.

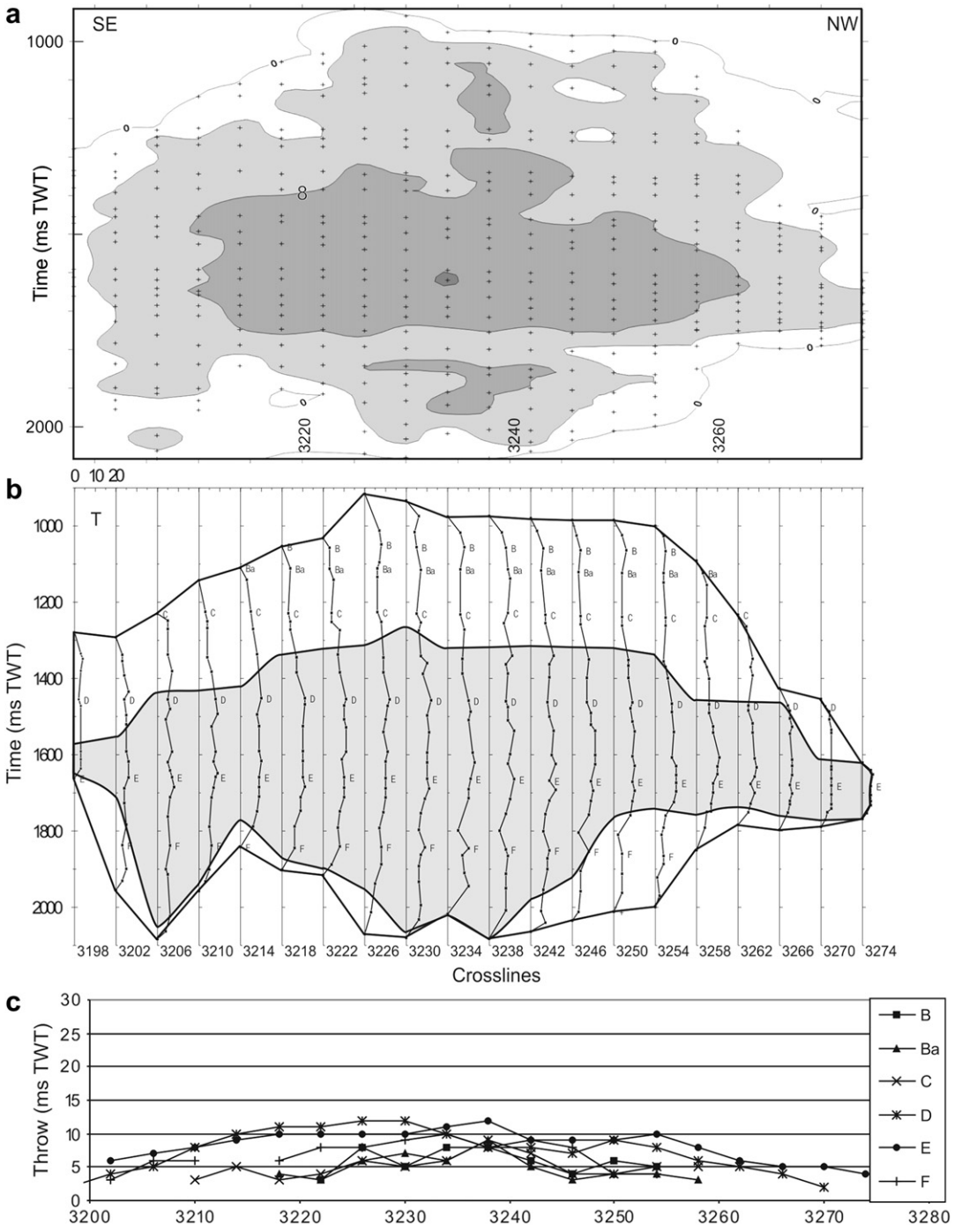

Fig. 6. Throw distribution for Fault 17. (a) Throw contour plot using 410 measurements along the fault length. Interval between crosslines is c. 50 m. Throw contours are spaced every 4 ms TWT. Dark colours indicate greater throw values (Tmax = 12 ms TWT). (b) Vertical throw-distribution graph showing T–z plots every 4 crosslines (c. 50 m). Each T–z plot represents the throw value (T) up to 20 ms TWT plotted against z in ms TWT. The blank area represents the tip folding surrounding the part of the fault plane that exhibits clear stratigraphic offset (shaded area). Key horizons are labelled B–F. (c) Graph showing the lateral throw distribution for 6 of the key horizons.

shallower above the YMM towards the lateral tip regions (see example in Figs. 7b,c and 8b).

Tip folds surrounding the unrestricted fault (Fault 17) with mostly a reverse-drag style have wavelengths greater than 200 m and amplitudes smaller than c. 5 ms TWT (Fig. 5d). The faults interpreted as restricted are characterised by larger wavelength and greater amplitude reverse-drag folds that are mostly localised on fault portions in contact with the YSM or the Messinian evaporites (Figs. 7a,d, 8b, 10b and 11b).

The upper portions of all case-study fault planes show transitions from discrete fault offset of reflections to fold-like deflections of reflections with a normal-drag geometry that is consistent with an interpretation of fault propagation folding (Figs. 5b, 7a and 9). While these deflections could

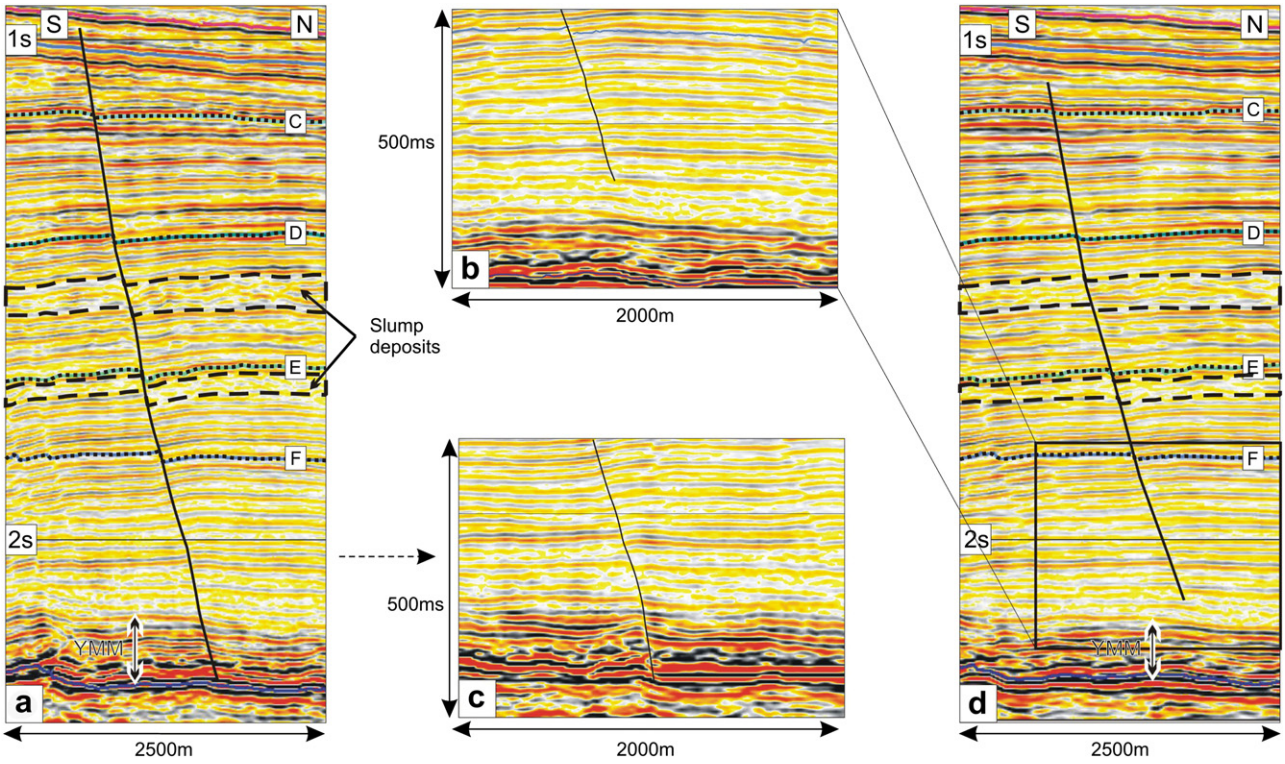

Fig. 7. Seismic section across Fault 19. (a) Crossline 2856 showing the fault geometry in the central part where the lower-tip terminates in the YMM and Messinian evaporites. Dotted lines represent key horizons; dashed lines indicate slump deposits. (b) Close-up of the lower-tip in the lateral region (crossline 2836) terminating above the YMM and the Messinian evaporates. (c) Close-up of the lower-tip in the central region (crossline 2892) terminating within the YMM. (d) Crossline 2836 showing the fault geometry in the lateral region.

result from closely spaced sub-seismic synthetic faults or folding during lateral-tip propagation (e.g. Cartwright and Mansfield, 1998); experimental, field-based and seismic-based studies show that upper-tip folding occurs ahead of propagating normal faults (e.g. Gawthorpe et al., 1997; Patton et al., 1998; Hardy and McClay, 1999; Withjack and Callaway, 2000; Jackson et al., 2006). The consideration of the deflections is essential as they constitute a considerable proportion of the fault-surface area varying from 10% for Fault 19 (Fig. 8) to over 30% for Faults 17 and 21 (Figs 6 and 9) within the limits of the seismic resolution. The region of tip folding covers the upper 10% of the fault for Fault 15/16, but extends downward to encompass 30% of the total height towards the lateral tips and adjacent to the relay zone (Fig. 10).

5. Throw analysis

Vertical throw distribution plots (T–z) were constructed for the case study faults along closely spaced seismic sections (50–250 m). The high frequency content of the seismic data meant that vertical throw measurements could be made at closely spaced intervals of c. 20–30 m, allowing subtle changes in throw gradient to be observed. Throw contour projections were constructed from these measurements and illustrate the throw distribution on fault planes. Lateral throw distribution plots were constructed for key horizons as a further means for analysing distribution.

5.1. Fault 17

The pattern of throw distribution for the whole fault plane (Fig. 6a) is characterised by an elliptical outline and throw contours approximately centred on a large maximum throw zone of 12 to 13 ms TWT (c. 11 m).

The vertical throw distribution plots for Fault 17 exhibit mostly flat-topped profiles (M-type of Muraoka and Kamata, 1983) with some degrees of variation (Fig. 6b). The central section of most of the plots (40–95% of the fault height) shows little throw variation, characterised by very small gradients (<0.05 with an average of 0.023). The extreme upper and lower-tip regions of the fault (covering between 5% and 10% of the fault surface area) exhibit throw gradients ranging from 0.03 to 0.3 (average c. 0.08). Throw gradients obtained for these tips regions are subject to uncertainty as a function of true tip positions due to the limits of seismic resolution.

Some irregularities in the throw profile are attributed to local changes in lithology, such as the local decrease in throw value located at 1800 ms TWT, which corresponds to a thin package of continuous high amplitude reflections (Fig. 5a). Interestingly, the basal tip is irregular in shape, and is shallowest between crosslines 3210 and 3222, where the lower-tip region is embedded in this same package of high amplitude reflections.

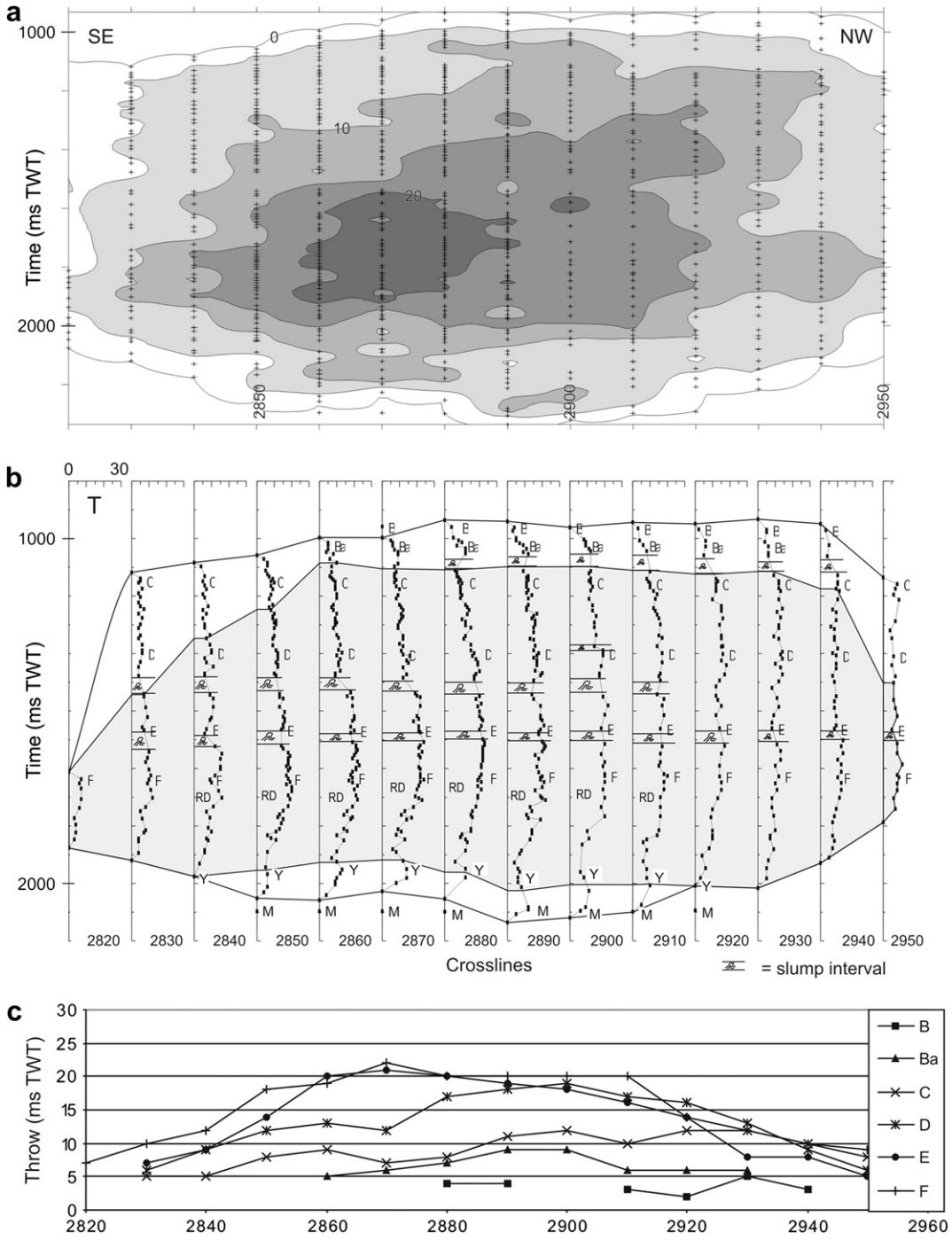

Fig. 8. Throw distribution for Fault 19. (a) Throw contour plot showing lines of equal throw value every 5 ms TWT. Eight hundred and nine throw values were measured on 14 seismic sections equally spaced at 125 m. Greater throw values (>20 ms TWT) are expressed as dark colours. (b) Vertical throw distribution every 10 crosslines (c. 125 m). Each T−z plot represents the throw value (T) up to 30 ms TWT plotted against z in ms TWT. Blank area represents the tip folding surrounding the fault. Reverse-drag folding (RD) is observed in the part of the fault that accumulated the most displacement. B, Ba, C, D, E and F are mapped Pleistocene horizons. Y and M are respectively the top of the Yafo Marls Member and the top of the Messinian evaporites.

Lateral throw distribution is mostly characterised by flat-topped profiles for the key horizons (Fig. 6c). The throw values exhibit very small variations over the broad central region and decrease uniformly towards the lateral tips. All lateral throw profiles are closely spaced and illustrate further the small difference in throw values between the mapped horizons.

5.2. Fault 19

The throw distribution on Fault 19 exhibits quasi elliptical contours with the long axis along strike centred on a large region of maximum throw with values up to 24 ms TWT (c. 21 m) (Fig. 8a). The throw contours are more closely spaced on the lower part of the fault plane than on the upper part.

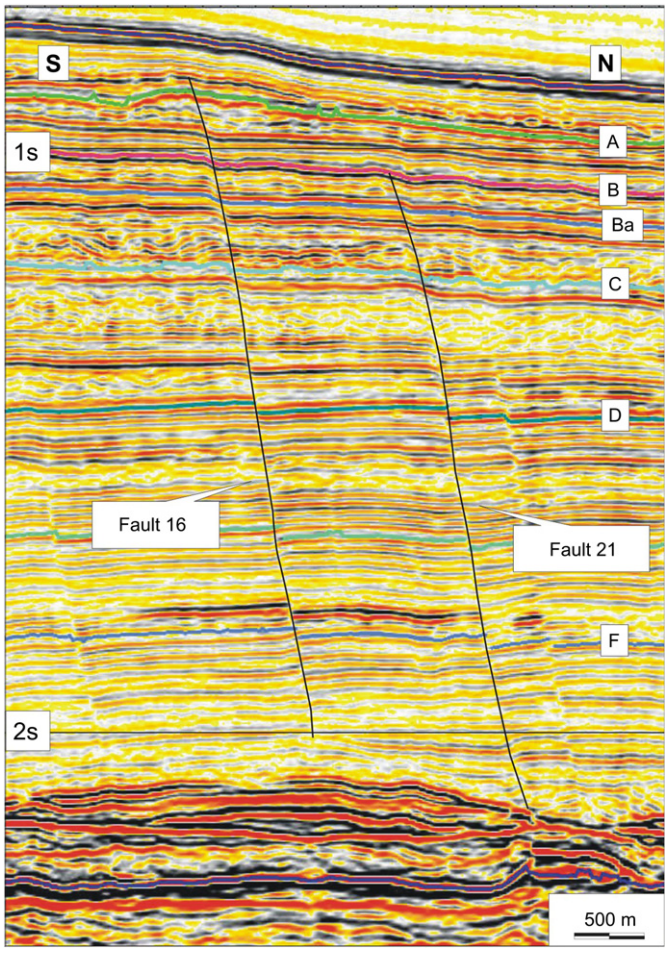

Fig. 9. Seismic cross section showing locations and geometries of Faults 16 and 21.

The vertical throw distribution for Fault 19 exhibits mainly flat-topped profiles (M type) with constant throw values over a major part of the fault height (e.g. crossline 2940 on Fig. 8b). However, in the central region of the fault, where the basal tip occurs within the YMM, the T–z plots exhibit an increase of throw values over the entire height and especially over the lower half of the fault plane. As a result, the throw profiles tend to be an asymmetrical C-type. Where the fault tips out even deeper, within the Messinian evaporites (crosslines 2890 to 2910), the vertical throw distribution is again characterised by flat-topped profiles. Therefore, variations in the throw distribution pattern depends on the stratigraphic unit in which the basal tip is located, indicating a first-order control by the mechano-stratigraphy as suggested in previous studies (e.g. Nicol et al., 1996; Gross et al., 1997; Nicol et al., 2003). Throw gradients are generally small along most of the fault plane (0.004 to 0.03 in the upper part and 0.01 to 0.06 in the lower part), but dramatically increase (by c. 50%) close to the lower-tip regions.

Lateral throw distribution is characterised by hybrid profiles between triangular and flat-topped profiles for Fault 19. Flat-topped profiles are observed for horizons situated in the upper part of the fault plane (B, Ba and C) whereas horizons located in the central and lower half of the fault exhibit more triangular profiles (i.e. D and E). Lateral profiles are widely spaced with deeper horizons characterised by higher throw values.

The influence of lithology on throw distribution can be seen at several places on Fault 19 and relates to the distribution of slump units within this mudstone succession. Firstly, an abrupt change in throw gradient between Horizons D and E separates the upper half of the fault plane, which exhibits small throw values and gradients (c. 0.015) from the lower half of the fault plane and its greater throw values. This interval of change in the throw profile is characterised on the seismic by a package of discontinuous, low amplitude reflections interpreted regionally as slump deposits (Frey Martinez et al., 2005). Secondly, another slump interval is interpreted at c. 1700 ms TWT that only corresponds to a minor inflection in the throw profiles. Thirdly, the limit between the zone of upper-tip folding and seismically resolvable systematic offset generally corresponds to the base of the slumped interval located at c. 1100 ms TWT.

5.3. Fault 15/16

The throw contours for Fault 15/16 are elliptical in shape, concentric and centred on the two zones of maximum throw located at the middle of the two segments (Fig. 10a). The greatest throw gradients occur in the lower part of the fault plane. A sub-vertical zone of minimal throw values separates the two segments as expected for fault linkage (e.g. Peacock and Sanderson, 1991; Walsh and Watterson, 1991).

The vertical throw distribution for Fault 15/16 is mainly characterised by flat-topped (M type) patterns and small throw gradients (c. 0.01) in the relay zone and at lateral tip regions where the basal tip is located several tens or hundreds of metres above the YSM (Fig. 10b). The central parts of both segments tip-out downward at the top of the YSM, and are asymmetric and triangular with greater gradients in the lower-tip region (up to 0.04 in the upper half and 0.07 in the lower part). This distribution is interpreted to result from mechanical control on throw distribution of a major part of the fault plane.

All lateral throw profiles except for Horizon B are characterised by triangular distributions for both fault segments (15 and 16) separated by an area of lesser throw values in the location of the relay zone (Fig. 10c). Deeper horizons (D, E, F) have greater throw values than shallower horizons (B, Ba, C).

5.4. Fault 21

Throw contours illustrate a major zone of throw maxima (centred on crossline 3180 and up to 24 ms TWT) separated by a zone of throw minima from a smaller maximum (centred on crossline 3140) (Fig. 11a). These two regions of throw maxima are surrounded by throw contours with a horizontal elongate shape. This pattern is interpreted to result from the hard linkage of two fault segments (Walsh and Watterson, 1991; Nicol et al., 1996).

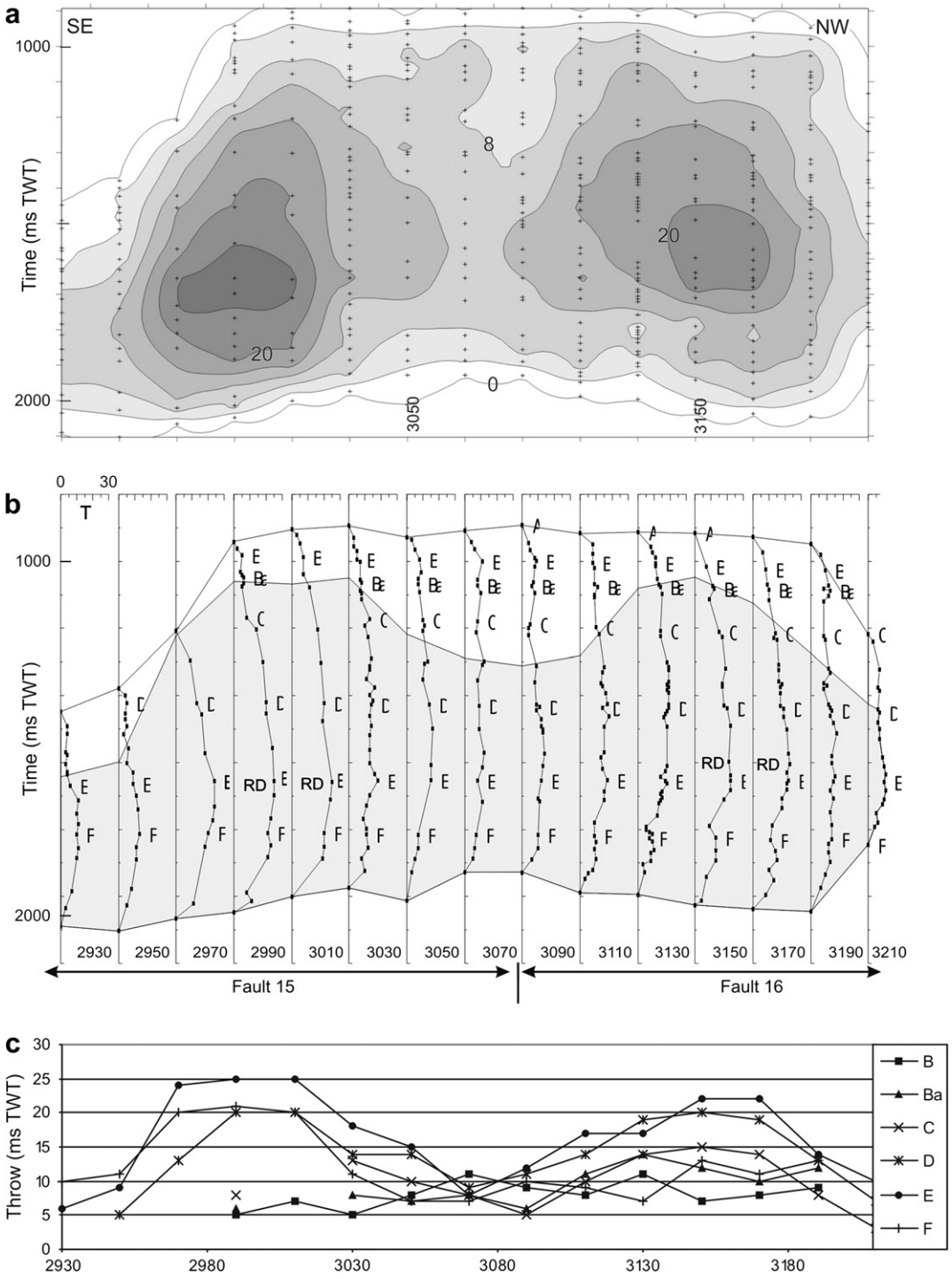

Fig. 10. Throw distribution for Fault 15/16. (a) Throw strike projection plot with contours spaced every 4 ms TWT. Crosses indicate the 446 measurements presented every 20 crosslines (c. 250 m). (b) Vertical throw distribution plots where each T–z plots represents the throw values (T) up to 30 ms TWT plotted against time (z). Shaded area is faulted and blank area is upper-tip folding. RD indicates reverse-drag folding associated to this part of the fault. (c) Lateral throw profiles for key horizons.

The vertical throw distribution of Fault 21 varies considerably along the fault trace. Flat-topped patterns characterise the lateral tip regions (Fig. 11b). Hybrid profiles are seen on crosslines 3120, 3140 and 3200. Asymmetric triangular throw profiles are only observed in the central-NW part of the fault (crosslines 3160 and 3180) where the fault tips out at the top of the YSM. This part of the fault accumulated the most displacement and is characterised by greater throw gradients (up to 0.12).

Lateral throw profiles are mostly asymmetrical and triangular and are characterised by a small deficit in the area between crosslines 3140 and 3160, which is interpreted as a breached relay zone (Fig. 11c).

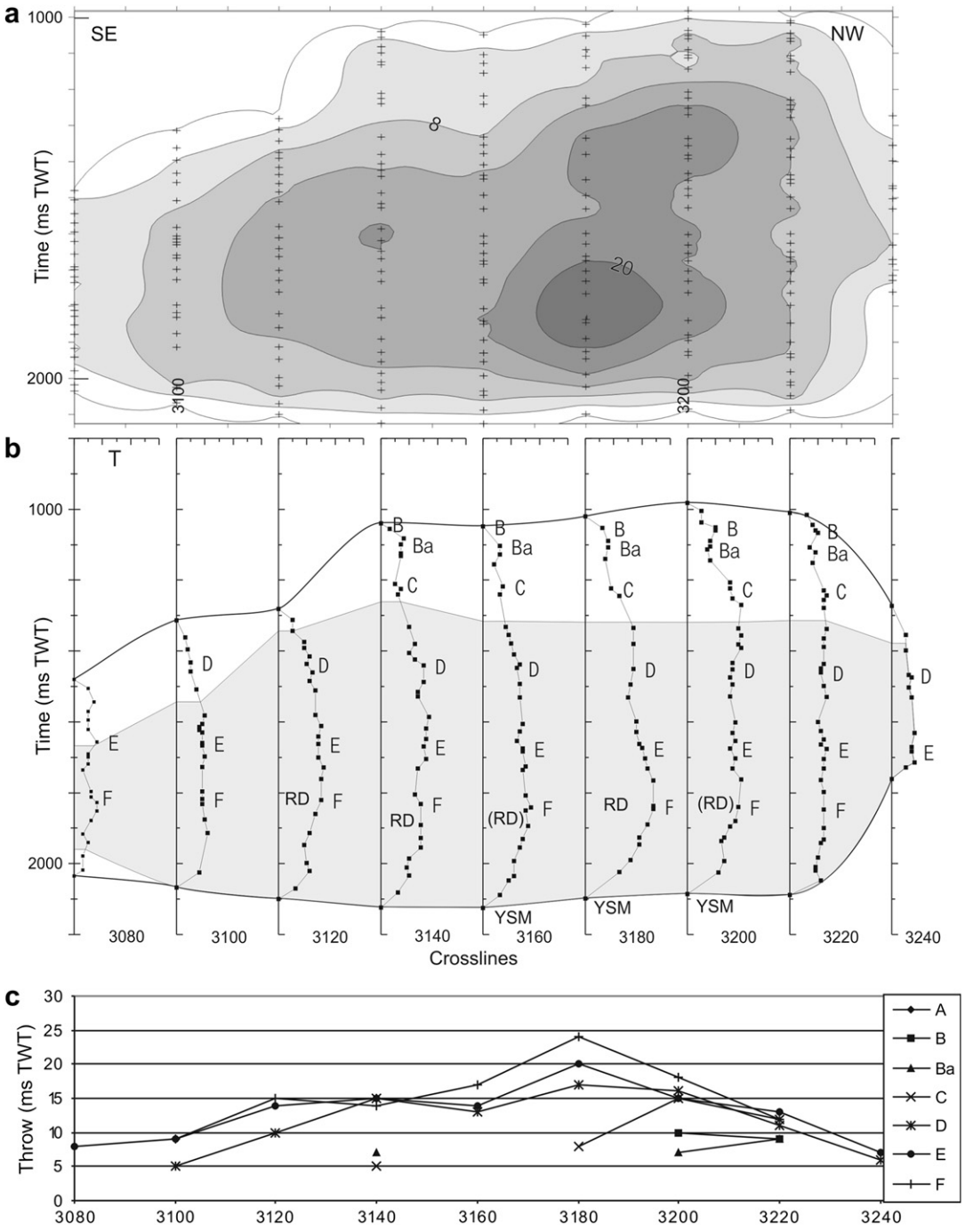

Fig. 11. Throw distribution for Fault 21 based on 234 measurements and presented every 20 crosslines (c. 250 m). (a) Throw contour plot with lines of equal throw values spaced every 4 ms TWT. (b) T–z plots (T) showing the throw values up to 30 ms TWT. B, Ba, C, D, E, F and Yafo Sand Member (YSM) are mapped horizons. RD is reverse-drag folding, in parentheses indicating small amplitude. (c) Lateral throw profiles for key horizons.

6. Discussion

6.1. Criteria for recognition of blind faults

Synsedimentary faults can be characterised by throw patterns very similar to those of blind faults (e.g. Petersen et al., 1992; Childs et al., 1993; Nicol et al., 1996). In addition, a fault may have both synsedimentary and post-sedimentary displacement components. Based on the original definition of blind faults (Watterson, 1986), we suggest using the combination of three criteria when assessing whether or not a fault is blind: (1) plunging upper-tip region geometry, including the tip line and adjacent displacement contours, (2) presence and geometry of upper-tip propagation folds, and (3) absence of clear geomorphological/stratigraphic indicators of synsedimentary fault activity.

6.1.1. Tip zone plunge

The geometry of the upper-tip line and throw contours can be used to positively identify blind faults. It has been suggested that post-sedimentary portions on faults are characterised by concentric throw contour pattern and synsedimentary parts by predominantly horizontal contours (Childs et al., 1993, 2003; Nicol et al., 1996). According to this view, a blind fault that subsequently propagated to the surface exhibits an abrupt change in the throw contours from sub-vertical to sub-horizontal between the post- and synsedimentary parts of a fault, respectively. However, this clear demarcation between sub-vertical and horizontal contours only develops when a significant proportion of the total displacement accrued whilst the fault was synsedimentary, which limits this approach when analysing the growth history of minor faults.

We suggest that where data quality permits good resolution of the geometry of the upper-tip line, then significant plunge of the tip-line and adjacent contours are diagnostic indicators. A tip line plunging down from the central part of a fault plane towards the lateral tip regions, cutting significantly the stratigraphy as it does so, suggests that the fault is blind. A rare potential pitfall to this approach is that similarly plunging tip-lines could occur where faults intersecting the free surface are retreated (Meyer et al., 2002).

Considering Fault 17 as an example, the upper-tip region plunges down several hundreds of metres from the central part towards the lateral tip regions (Fig. 6b). Stratigraphically, the fault tips out upward in the central part c. 350 m above the stratigraphic level of the lateral tip-lines, which is equivalent to over a million years of sediment deposition. Were the fault synsedimentary rather than blind, then this tip-region geometry would imply that the fault firstly propagated to its maximum length at the depositional surface, and then continued activity over a million years or so with a steadily decreasing portion of the fault surface actively displacing through time, such that the active portion of the fault intersecting the free surface retreated towards the fault centre with continued growth. Although not impossible, this scenario is much more complex than the alternative of a blind propagating tip-line with elliptical geometry, and is also generally counter to models of fault growth that predict fault lengthening with increasing displacement (e.g. Walsh and Watterson, 1988a; Cowie and Scholz, 1992; Dawers et al., 1993).

The same observation applies to the throw analysis for Fault 19 (Fig. 8b). If the propagation fold is excluded, the upper-tip line plunges c. 600 m vertically over a distance of 500 m towards the SE lateral tip. Fault 15/16 exhibits the same tip-line geometry, with a plunge of c. 300 m vertically over a distance of c. 900 m (Fig. 10b). The upper-tip geometry of Fault 21 (Fig. 11b) is not considered because it was influenced by interaction with Fault 20 (cf. Segall and Pollard, 1980).

While tip-line plunge can be indicative of blind faulting, however, the identification of blind faults based on upper-tip line plunge alone is insufficient because of seismic resolution limitations and the possibility that a seismically resolvable tip-line is not the true tip-line.

6.1.2. Upper-tip propagation fold

Upper-tip folding in a monoclinal style is frequently associated with upward propagation of blind normal faults (e.g. Gawthorpe et al., 1997; Patton et al., 1998; Hardy and McClay, 1999; Withjack and Callaway, 2000; Jackson et al., 2006). Given sufficient seismic resolution to distinguish this type of folding from imaging artefacts, the presence of systematic tip folds beneath the upper-tip line is regarded as a criterion for recognising blind faults. Upper-tip folds have also been described on growth faults (e.g. Gawthorpe et al., 1997) but the fold wavelength above growth faults is generally greater than observed in the El Arish array. The recognition of upper-tip folds was possible because of the very good spatial and vertical resolution relative to the scale of the offsets or fold amplitudes. Poorer quality seismic data may not distinguish systematic offset of unfolded strata (fault offsets) from short wavelength tip-fold (Walsh and Watterson, 1987). Hence, the use of this criterion is dependent on scale and data quality, and should be used in combination with the others.

6.1.3. Absence of evidence of synsedimentary faulting

Synsedimentary faults commonly have growth packages with significant thickening in the hangingwall (e.g. Wadsworth, 1953; Hardin and Hardin, 1961; Thorsen, 1963). However, many small synsedimentary faults with low expansion factors are much harder to recognise (Childs et al., 2003), so it may be impossible to determine whether they are synsedimentary or blind. An array of faults is in some ways easier to analyse. For example, if all faults in an array tip-out upward at a single horizon that is not mechanically important, it is very likely that the faults were synsedimentary rather than blind.

The upper-tips of different faults of the El Arish terminate at different stratigraphic levels. Given the distribution and close spacing of faults in the array, we interpret them as blind faults that propagated upward to different levels rather than synsedimentary faults buried at such a range of stratigraphic levels. Their current upper-tip-line positions lack temporal significance.

It was noted above that for the case study faults there is no obvious stratigraphic thickening in the hangingwall of any fault. The absence of evidence of fault interaction with the seabed, such as a change in the shape, size or direction of slope channels or mass transport complexes also supports the interpretation that these faults are blind. However, the extent to which synsedimentary faults can potentially impact the surface morphology and sediment transport patterns is governed by slip rate versus sedimentation rate (Edwards, 1995; Cartwright et al., 1998; Castelltort et al., 2004), so the absence of these indicators can sometimes be due to resolution and scale problems rather than to the lack of surface interaction. For this reason, this criterion should be used in conjunction with the other two.

6.2. Lithological barrier controls

The importance of mechanical stratigraphy is emphasised in recent studies where lithological boundaries acted as

barriers to fault propagation (Rippon, 1985; Gross, 1995; Childs et al., 1996a; Nicol et al., 1996; Wilkins and Gross, 2002). Generally, when a fault abuts against a mechanical barrier, its propagation is restricted, and displacement gradients increase as additional slip accrues adjacent to the barrier. This displacement increase is thought to provide the additional strain necessary for fault propagation through the barrier (Nicol et al., 1996; Gupta and Scholz, 2000; Wilkins and Gross, 2002). We recognise a number of examples of mechano-stratigraphic influences on propagation such as the change in throw profile for faults that are restricted at their lower-tip regions. The unrestricted fault presented in this study (Fault 17, Fig. 5) is characterised by flat-topped throw profiles and similar throw gradients at lower and upper-tips (Fig. 6b) whereas restricted faults (Faults 15/16, 19 and 21) exhibit more aymmetrical linear throw profiles. Other lithological barriers have been interpreted from the throw profile analyses. The faults of the El Arish array offset slump deposits (Frey Martinez et al., 2005) without changing geometry and orientation. However, the slump intervals coincide with changes in the throw distribution on the faults. Fault 19 illustrates the effect of slump intervals on the throw distribution (Fig. 8b). Most slump intervals correspond to an upward decrease in throw values, especially in the central part of the fault plane (i.e. crosslines 2850 to 2870 in Fig. 8b). Upward decreases in throw values on Fault 19 are interpreted to result from restriction when the fault propagated through slump deposit intervals, acting as mechanical barriers. The boundary between folding and faulting at the upper-tip corresponds to the base of a slump deposit, which we interpret to result from a mechanical stratigraphic barrier controlling the spatial distribution of tip-folding.

6.3. Throw distribution patterns on the fault planes

Most previous studies analysing throw distribution patterns on normal faults used strike projection of throw contour plots (e.g. Rippon, 1985; Walsh and Watterson, 1988b, 1991; Nicol et al., 1996, 2003) and lateral throw profiles mostly derived from fault scarps or by measuring the throw variation of a horizon along strike (e.g. Peacock and Sanderson, 1991; Dawers et al., 1993; Peacock and Sanderson, 1994; Cartwright and Mansfield, 1998; McLeod et al., 2000; Morley and Wonganan, 2000; Nicol et al., 2005). Simple blind normal faults, in the absence of barriers and strong interaction with others faults are expected to exhibit a linear lateral displacement profiles also called C-shape or triangular (Muraoka and Kamata, 1983; Peacock and Sanderson, 1991; Nicol et al., 1996; Manighetti et al., 2001). Examples of vertical throw distribution are less common (e.g. Muraoka and Kamata, 1983; Childs et al., 1996b; Mansfield and Cartwright, 1996), mostly because a wider range of scales is available for horizontal rather than vertical fault traces from outcrop studies and because analysis of lateral throw distribution are less subject to lithological variations (e.g. Nicol et al., 1996, 2003; Gross et al., 1997; Wilkins and Gross, 2002).

In contrast to the expectation that displacement profiles should be C-shaped or triangular, a fundamental observation from the El Arish faults is that peaked C-type or triangular throw profile were not observed from the vertical profiles. Most T–z plots, instead, exhibit hybrid patterns with a broad central region and very gentle throw gradients. Fault 17, an unrestricted fault, exhibits vertical and lateral throw distribution that are flat-topped profiles with very small throw values and gradients (Fig. 6b and c). The significance of flat-topped (M-type) throw profiles was attributed to constant wall-rock strain in intervals of stiff materials (Muraoka and Kamata, 1983). This cannot explain the throw distribution for the faults from the El Arish array as they offset layered claystone-dominated siliciclastic sequences and the unrestricted faults are characterised by flat-topped profiles. We suggest that the flat-topped profiles of the unrestricted fault of the El Arish array are due to a rapid establishment of the fault dimension as already seen in other settings (Walsh et al., 2002), and that accumulation of displacement on the neighbouring restricted faults are due to interaction with mechanical boundaries during propagation.

7. Conclusions

1. This study provided a detailed analysis of the geometry and displacement distribution for unrestricted and restricted blind faults from 3D seismic data located in the Levant Basin. Blind faults are defined herein as post-sedimentary faults that show no evidence of interaction with the free surface at any time during evolution.
2. Three main criteria are suggested to help the recognition of blind faults from 3D seismic data: (1) plunging upper-tip line and throw contours geometry, (2) presence of upper-tip propagation folds, and (3) absence of stratigraphic evidences of the fault intersecting the free surface.
3. The throw analysis is presented for four case study faults with throw contour, lateral and vertical profiles. Unrestricted faults do not exhibit striking triangular (linear or C type) throw profile as expected for blind faults but are mostly characterised by flat-topped profiles.
4. The throw distribution for restricted blind faults is greatly influenced by fault interaction with lithological boundaries acting as mechanical barriers. Vertical profiles are more commonly C-type in parts of the faults that are restricted and flat-topped profiles are preserved in unrestricted regions.

Acknowledgements

We wish to thank BG-Group for supplying the seismic data and for permission to publish this work. In particular, help from Paul Griffiths is greatly appreciated. Brent Couzens-Shultz, John Walsh and Bill Dunne are thanked for thoughtful and constructive reviews. Schlumberger Ltd is acknowledged for providing Geoquest seismic interpretation software.

References

Barnett, J.A.M., Mortimer, J., Rippon, J.H., Walsh, J.J., Watterson, J., 1987. Displacement geometry in the volume containing a single normal fault. American Association of Petroleum Geologists Bulletin 71 (8), 925–937.

Bertoni, C., Cartwright, J.A., 2006. Controls on the basinwide architecture of late Miocene (Messinian) evaporites on the Levant margin (Eastern Mediterranean). Sedimentary Geology 188–189, 93–114.

Cartwright, J.A., Jackson, M.P.A., 2008. Initiation of gravitational collapse of an evaporite basin margin: the Messinian saline giant, Levant Basin, Eastern Mediterranean. Geological Society of America Bulletin 120 (3–4), 399–413.

Cartwright, J.A., Mansfield, C.S., 1998. Lateral displacement variation and lateral tip geometry of normal faults in the Canyonlands National Park, Utah. Journal of Structural Geology 20 (1), 3–19.

Cartwright, J.A., Truddgill, B.D., Mansfield, C.S., 1995. Fault growth by segment linkage: an explanation for scatter in maximum displacement and trace length data from the Canyonlands Grabens of SE Utah. Journal of Structural Geology 17 (9), 1319–1326.

Cartwright, J.A., Bouroullec, R., James, D., Johnson, H.D., 1998. Polycyclic motion history of some Gulf Coast growth faults from high-resolution displacement analysis. Geology 26 (9), 819–822.

Castelltort, S., Pochat, S., Van Den Driessche, J., 2004. Using T-Z plots as a graphical method to infer lithological variations from growth strata. Journal of Structural Geology 26 (8), 1425–1432.

Childs, C., Easton, S.J., Vendeville, B.C., Jackson, M.P.A., Lin, S.T., Walsh, J.J., Watterson, J., 1993. Kinematic analysis of faults in a physical model of growth faulting above a viscous salt analogue. Tectonophysics 228, 313–329.

Childs, C., Nicol, A., Walsh, J.J., Watterson, J., 1996a. Growth of vertically segmented normal faults. Journal of Structural Geology 18 (12), 1389–1397.

Childs, C., Watterson, J., Walsh, J.J., 1996b. A model for the structure and development of fault zones. Journal of the Geological Society, London 153 (3), 337–340.

Childs, C., Nicol, A., Walsh, J.J., Watterson, J., 2003. The growth and propagation of synsedimentary faults. Journal of Structural Geology 25, 633–648.

Cowie, P.A., Scholz, C.H., 1992. Growth of faults by accumulation of seismic slip. Journal of Geophysical Research 97 (B7), 11085–11095.

Dawers, N.H., Anders, M.H., 1995. Displacement-length scaling and fault linkage. Journal of Structural Geology 17 (5), 607–614.

Dawers, N.H., Anders, M.H., Scholz, C.H., 1993. Growth of normal faults: Displacement-length scaling. Geology 21, 1107–1110.

Druckman, Y., Buchbinder, B., Martinotti, G.M., Tov, R.S., Aharon, P., 1995. The buried Afiq Canyon (eastern Mediterranean, Israel): a case study of a Tertiary submarine canyon exposed in Late Messinian times. Marine Geology 123 (3–4), 167–185.

Edwards, M.B., 1995. Differential subsidence and preservation potential of shallow-water Tertiary sequences, northern Gulf Coast Bain, USA. In: Plint, A.G. (Ed.), Sedimentary Facies Analysis. International Association of Sedimentologists Special Publication, 22, pp. 265–281.

Frey Martinez, J., Cartwright, J.A., Hall, B., 2005. 3D seismic interpretation of slump complexes: examples from the continental margin of Israel. Basin Research 17, 83–108.

Garfunkel, Z., 1998. Constrains on the origin and history of the Eastern Mediterranean basin. Tectonophysics 298 (1–3), 5–35.

Garfunkel, Z., Almagor, G., 1987. Active Salt Dome Development in the Levant Basin. Southeast Mediterranean. Academic Press, Orlando, FL, 263-300 pp.

Gawthorpe, R.L., Sharp, I., Underhill, J.R., Gupta, S., 1997. Linked sequence stratigraphic and structural evolution of propagating normal faults. Geology 25 (9), 795–798.

Gillespie, P.A., Howard, C.B., Walsh, J.J., Watterson, J., 1993. Measurement and characterisation of spatial distributions of fractures. Tectonophysics 226, 113–141.

Gradmann, S., Hubscher, C., Ben-Avraham, Z., Gajewski, D., Netzeband, G., 2005. Salt tectonics off northern Israel. Marine and Petroleum Geology 22 (5), 597–611.

Gross, M.R., 1995. Fracture partitioning: Failure mode as a function of lithology in the Monterey Formation of coastal California. Geological Society of America Bulletin 107 (7), 779–792.

Gross, M.R., Gutierrez-Alonso, G., Bai, T., Wacker, M.A., Collinsworth, K.B., Behl, R.J., 1997. Influence of mechanical stratigraphy and kinematics on fault scaling relations. Journal of Structural Geology 19 (2), 171–183.

Gupta, A., Scholz, C.H., 2000. A model of normal fault interaction based on observations and theory. Journal of Structural Geology 22, 865–879.

Hardin, F.R., Hardin, G.C.J., 1961. Contemporaneous normal faults of gulf coast and their relation to flexures. Bulletin of the Association of American Petroleum Geology 45 (2), 238–246.

Hardy, S., McClay, K., 1999. Kinematic modelling of extensional fault-propagation folding. Journal of Structural Geology 21 (7), 695–702.

Jackson, M.P.A., 1995. Retrospective salt tectonics. In: Jackson, M.P.A., Roberts, D.G., Snelson, S. (Eds.), Salt Tectonics, A Global Perspective. American Association of Petroleum Geologists Memoir, 65, pp. 1–28.

Jackson, C.A.L., Gawthorpe, R.L., Sharp, I.R., 2006. Style and sequence of deformation during extensional fault-propagation folding: examples from the Hammam Faraun and El-Qaa fault blocks, Suez Rift, Egypt. Journal of Structural Geology 28 (3), 519–535.

Maerten, L., Willemse, E.J.M., Pollard, D.D., Rawnsley, K., 1999. Slip distributions on intersecting normal faults. Journal of Structural Geology 21, 259–271.

Manighetti, I., King, G.C.P., Gaudemer, Y., Scholz, C.H., Doubre, C., 2001. Slip accumulation and lateral propagation of active normal faults in Afar. Journal of Geophysical Research 106 (B7), 13667–13696.

Mansfield, C.S., 1996. Fault Growth by Segment Linkage. PhD thesis, University of London.

Mansfield, C.S., Cartwright, J.A., 1996. High resolution fault displacement mapping from three-dimensional seismic data: evidence for dip linkage during fault growth. Journal of Structural Geology 18 (2/3), 249–263.

McLeod, A.E., Dawers, N.H., Underhill, J.R., 2000. The propagation and linkage of normal faults: insights from the Strathspey-Brent-Statfjord fault array, northern North Sea. Basin Research 12 (3–4), 263–284.

Meyer, V., Nicol, A., Childs, C., Walsh, J.J., Watterson, J., 2002. Progressive localisation of strain during the evolution of a normal fault population. Journal of Structural Geology 24 (8), 1215–1231.

Morley, C.K., Wonganan, N., 2000. Normal fault displacement characteristics, with particular reference to synthetic transfer zones, Mae Moh mine, northern Thailand. Basin Research 12 (3–4), 307–327.

Muraoka, H., Kamata, H., 1983. Displacement distribution along minor fault traces. Journal of Structural Geology 5 (5), 483–495.

Netzeband, G.L., Hubscher, C.P., Gajewski, D., 2006. The structural evolution of the Messinian evaporites in the Levantine Basin. Marine Geology 230 (3-4), 249–273.

Nicol, A., Watterson, J., Walsh, J.J., Childs, C., 1996. The shapes, major axis orientations and displacement patterns of fault surfaces. Journal of Structural Geology 18 (2/3), 235–248.

Nicol, A., Walsh, J.J., Watterson, J., Nell, P.A.R., Bretan, P., 2003. The geometry, growth and linkage of faults within a polygonal fault system from South Australia. In: Geological Society, London, Special Publications 216. Geological Society, London (1)245–261.

Nicol, A., Walsh, J., Berryman, K., Nodder, S., 2005. Growth of a normal fault by the accumulation of slip over millions of years. Journal of Structural Geology 27 (2), 327–342.

Patton, T.L., Logan, J.M., Friedman, M., 1998. Experimentally generated normal faults in single-layer and multilayer limestone specimens at confining pressure. Tectonophysics 295 (1–2), 53–77.

Peacock, D.C.P., Sanderson, D.J., 1991. Displacements, segment linkage and relay ramps in normal fault zones. Journal of Structural Geology 13 (6), 721–733.

Peacock, D.C.P., Sanderson, D.J., 1994. Geometry and development of relay ramps in normal fault systems. AAPG 78 (2).

Peacock, D.C.P., Zhang, X., 1994. Field examples and numerical modelling of oversteps and bends along normal faults in cross-section. Tectonophysics 234, 147–167.

Petersen, K., Clausen, O.R., Korstgard, J.A., 1992. Evolution of a salt-related listric growth fault near the d-1 well, block 5605, Danish north sea: displacement history and salt kinematics. Journal of Structural Geology 14 (5), 565–577.

Rippon, J.H., 1985. Contoured patterns of the throw and hade of normal faults in the Coal Measures (Wesphalian) of the north-east Derbyshire. Proceedings of the Yorkshire Geological Society 45 (3), 147–161.

Segall, P., Pollard, D.D., 1980. Mechanics of discontinuous Faults. Journal of Geophysical Research 85 (B8), 4337–4350.

Thorsen, C.E., 1963. Age of growth faulting in the southeast Louisiana. Transactions of the Gulf Coast Association of Geological Societies 13, 103–110.

Tibor, G., Ben-Avraham, Z., 1992. Late Tertiary seismic facies and structures of the levant passive margin off central Israel, eastern Mediterranean. Marine Geology 105, 253–273.

Tibor, G., Ben-Avraham, Z., 2005. Late Tertiary paleodepth reconstruction of the Levant margin off Israel. Marine Geology 221 (1–4), 331–347.

Wadsworth, J.A.H., 1953. Percentage of thinning chart-new technique in subsurface geology. American Association of Petroleum Geologists Bulletin 37 (1), 158–162.

Walsh, J.J., Watterson, J., 1987. Distributions of cumulative displacement and seismic slip on a single normal fault surface. Journal of Structural Geology 9 (8), 1039–1046.

Walsh, J.J., Watterson, J., 1988a. Analysis of the relationship between displacements and dimensions of faults. Journal of Structural Geology 10 (3), 239–247.

Walsh, J.J., Watterson, J., 1988b. Dips of normal faults in British Coal Measures and other sedimentary sequences. In: Journal of the Geological Society, London, 145. 859–873.

Walsh, J.J., Watterson, J., 1991. Geometric and kinematic coherence and scale effects in normal fault systems. In: Roberts, A.M., Yielding, G., Freeman, B. (Eds.), The Geometry of Normal Faults. Geological Society of London, Special Publication, 56, pp. 193–203.

Walsh, J.J., Nicol, A., Childs, C., 2002. An alternative model for the growth of faults. Journal of Structural Geology 24, 1669–1675.

Watterson, J., 1986. Fault dimensions, displacements and growth. Pure and Applied Geophysics 124 (1/2), 365–373.

Watterson, J., Nicol, A., Walsh, J.J., Meier, D., 1998. Strains at the intersections of synchronous conjugate normal faults. Journal of Structural Geology 20 (4), 363–370.

Wilkins, S.J., Gross, M.R., 2002. Normal fault growth in layered rocks at Split Mountain, Utah: influence of mechanical stratigraphy on dip linkage, fault restriction and fault scaling. Journal of Structural Geology 24 (9), 1413–1429.

Withjack, M.O., Callaway, S., 2000. Active normal faulting beneath a salt layer: an experimental study of deformation patterns in the cover sequence. American Association of Petroleum Geologists Bulletin 84 (5), 627–651.

Wojtal, S.F., 1996. Changes in fault displacement populations correlated to linkage between faults. Journal of Structural Geology 18 (2–3), 265–279.